Towards the biomechanical modelling of the behaviour of ex-vivo porcine perineal tissues

Tiguida Kadiakhe, Marine Lallemant, Jérôme Chambert, Nicolas Mottet, Arnaud Lejeune, Emmanuelle Jacquet

Towards the biomechanical modelling of the behaviour of *ex-vivo* porcine perineal tissues

Tiguida Kadiaké[a], Marine Lallemant[a,b], Jérôme Chambert[a], Nicolas Mottet[b,c], Arnaud Lejeune[a], Emmanuelle Jacquet[a,*]

[a] *Université de Franche-Comté, CNRS, institut FEMTO-ST, 25000 Besançon, France*
[b] *Service de gynécologie obstétrique, CHU Jean Minjoz, 25000 Besançon, France*
[c] *Université de Franche-Comté, EA4662, laboratoire de Nanomédecine, 25000 Besançon, France*

Abstract

The perineum is a layered soft tissue structure with mechanical properties that maintain the integrity of the pelvic floor. During childbirth, the perineum undergoes significant deformation that often results in tears of various degrees of severity. To better understand the mechanisms underlying perineal tears, it is crucial to consider the mechanical properties of the different tissues that make up the perineum. Unfortunately, there is a lack of data on the mechanical properties of the perineum in the literature. The objective of this study is to partly fill these gaps. Hence sow perineums were dissected and the five perineal tissues involved in tears were characterized by uniaxial tension tests: Skin, Vagina, External Anal Sphincter, Internal Anal Sphincter and Anal Mucosa. From our knowledge, this study is the first to investigate all these tissues and to design a testing protocol to characterize their material properties. Six material models were used to fit the experimental data and the correlation between experimental and predicted data was evaluated for comparison. As a result, even if the tissues are of different nature, the best correlation was obtained with the Yeoh and Martins material models for all tissues. Moreover, these preliminary results show the difference in stiffness between the tissues which indicates that they might have different roles in the structure. These obtained results will serve as a basis to design an improved experimental protocol for a more robust structural model of the porcine perineum that can be used for the human perineum to predict perineal tears.

Keywords: Soft biological tissues, Hyperelasticity, Experimental tests, Biomechanical characterization, Perineum

1. Introduction

The female perineum is a complex multilayer structure composed of soft tissues located under the pelvic floor. On the most superficial layer we find the skin, vulva and vaginal opening. The deeper layers are composed of muscles, glands and the perineal body. Perineal tears are a common occurrence in vaginal births affecting up to 89% of women of which most are primiparous (Goh et al., 2018). Perineal tears can involve the skin around the vulva, the vagina, the

*Corresponding author: emmanuelle.jacquet@univ-fcomte.fr (E. Jacquet)

perineal body (central attachment of perineal muscles), the external and internal anal sphincter (EAS and IAS) and the anal mucosa (AM). It is known that the perineum provides a mechanical support to the pelvic floor and the pelvic organs (DeLancey, 1999; Larson et al., 2010; Shafik et al., 2005), but its mechanical properties are not yet fully understood. As the perineum is a multilayer structure, it requires the mechanical characterization of each layer that constitute the tissue. However, to the best to our knowledge, studies on the biomechanical behaviour of the perineum are limited and do not consider all the perineal tissues. These mainly consist of finite element models and numerical simulations of the perineal body and pelvic floor as well as some experimental data on the vagina (Brieu et al., 2016; Jing et al., 2012; Parente et al., 2008, 2010; Rubod et al., 2008; Ruiz-Zapata, 2018; Strauss et al., 2012; Zemčík et al., 2012). In these studies, the pelvic floor muscles and perineal body behaviour were described by hyperelastic material models such as (Mooney, 1940; Holzapfel et al., 2000; Martins et al., 1998). The studies gave an insight on the location of the maximum stretches and stresses of the pelvic floor during the second stage of labor. Models of the pelvic floor are created using MRI images from pregnant and non-pregnant women. However, the perineum and the perineal body, which are difficult to image, were not included although elastic stiffness data of the perineal body were obtained using shear wave elastography (Chen et al., 2015; Rostaminia et al., 2019). Since obtaining human tissue samples for research purposes is challenging and time-consuming, the pig was chosen in this first step of our work. Additionally, this study is exploratory and the results obtained will allow us to characterize the human tissues by reusing the designed protocol after studying the influence of environmental and testing conditions of the samples. Human and porcine tissues have many similarities. Debeer et al. (2013) showed great histological similarities between the different layers of pig and human skin. Furthermore, it confirmed the use of porcine skin for scientific research. Micro-indentation tests have also shown that the mechanical properties of porcine skin and those of human skin are of the same order (Ranamukhaarachchi et al., 2016). They clarified that it was preferable to use fresh porcine skin under high humidity conditions to the use of frozen human skin. Comparative studies between the porcine perineum and the human perineum have never been carried out. However, a study was performed on sheep vaginal tissues (Rubod et al., 2007) and used as a characterization protocol for human vaginal tissues (Rubod et al., 2008). Other tissues such as stomach (Friis et al., 2023), brain (MacManus et al., 2020), bones, cartilage, ligaments (Cone et al., 2017; Tan et al., 2015) and certain muscles have already been studied, proving the potential of using the porcine model to replace the human for the identification of constitutive laws. The aim of the present work was to investigate the biomechanical properties of the perineum by developing an experimental protocol and to select a constitutive model that describe the behaviour of the five perineal tissues that compose the perineum: Skin, Vagina, External Anal Sphincter (EAS), Internal Anal Sphincter (IAS) and Anal Mucosa (AM). The perineal body was not studied as it is absent in the porcine perineum.

2. Material and Methods

Tensile experimental tests are the most common way to conduct mechanical characterisation of soft biological tissues (Navindaran et al., 2023). These tests allow us to identify the elastic, viscous and rupture properties of tissues. A testing protocol is proposed here to characterize the different tissues of the sow perineum. First, a dissection technique is implemented to identify and to collect the different tissues: skin, vagina, EAS, IAS, AM and then the experimental characterization of the samples is carried out.

2.1. Dissection technique

The perineal structures used for this study were discarded parts collected from the local porcine slaughterhouse for food, which respects the animal bioethical norms. The sow breed was the French pork butcher's pig. The sows were multiparous and not pregnant at the time of death. The structures were collected from the slaughterhouse four to five days after death. They were refrigerated during the time before collection. In order to obtain samples in a reproducible way and preserve fiber integrity, a precise dissection method has been implemented and performed by an urogynecologist expert in anatomy of perineal tears. The instruments used were fine scissors and atraumatic forceps. No traction on the tissues was performed. A careful midline incision next to the vulvar area between the vaginal and anal openings was made. The external anal sphincter (EAS) was immediately identified and isolated. The perineal skin was dissected from the anus to the ventral extremity into two dorso-ventral samples (right and left). Next, the ventral part of the vagina was incised. A right and left vaginal samples were dissected on the rectovaginal septum side. Histologically, the vaginal sample included the vaginal wall composed of mucosa, lamina propria, muscularis and adventitia (Gruber et al., 2012). Then, the external anal sphincter was carefully dissected and sectioned at the lateral sides. Finally, the dorsal wall of the rectum and anus was incised. Two samples (right then left) of the anal mucosa (AM) and the internal anal sphincter (IAS) were obtained. Only the right samples on the right side were analyzed for the perineal skin, the perineal vagina, the perineal anal mucosa and the IAS. The left samples of these sows were analyzed in another study with non-comparable experimental conditions. The entire EAS was collected between the vagina and the anus. Fig. 1 shows the different tissues and their location. In total, 5 samples were tested for each tissue, making a total of 25 samples.

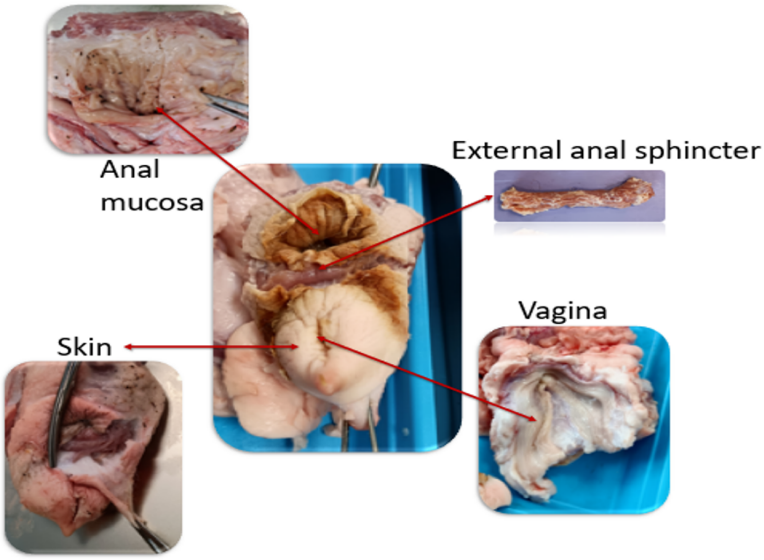

Figure 1: Anatomic description of perineal tissues. The sow perineum (in the middle) is dissected in 5 parts : Skin, Anal mucosa, vagina and External Anal Sphincter and Internal Anal Sphincter (not depicted here, located under the anal mucosa).

2.2. Test procedure

The samples were oriented using an indelible marker (right or cranial side depending on the part) before being studied. For each sample, a test sample was cut with a cold scalpel using a 5 cm $\times$ 1 cm rubber pre-made template. Paper was glued to the ends one centimeter from the edges to facilitate the gripping of the sample. The specimens were tested in quasi-static uniaxial tension at a velocity of 0.1 mm/s with the Mach-1 testing machine (Biomomentum Inc, Canada). The grips used are specific clamping grips for soft tissues to prevent slippage during tests. They consist of C-shaped cavities, coupled with stainless steel bars, screwed in place to solidly lock the sample in the grips. The displacement was imposed and the forces were measured with a 250 N force sensor. For each specimen, a pre-load of 0.3 N was applied before the test. Measurements of thickness, width and initial length were made once using a digital caliper after the pre-load at the center of the specimen. The mean thicknesses of the skin, vagina, external anal sphincter, anal mucosa and internal anal sphincter samples were respectively 3.15 ± 0.8 mm, 1.6 ± 0.6 mm, 4.5 ± 2.1 mm, 1.2 ± 0.2 mm, 2.7 ± 0.8 mm. The displacement (Δl) and the force were recorded with an accuracy of 0.5 μm and 12.5 μN at a frequency of 100 Hz. A sample of EAS installed in the grips can be seen in Fig. 2.

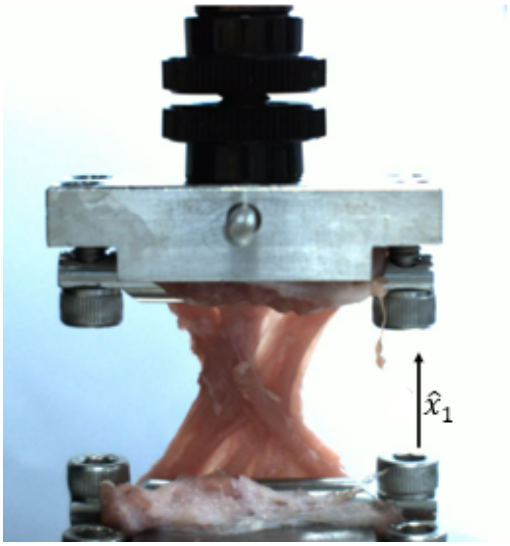

Figure 2: EAS installed in the grips after preload in the tension direction $\hat{x}_1$.

2.3. Identification of the hyperelastic constitutive law

Biological soft tissues behaviour results from nonlinear phenomena. These phenomena include time dependency and stress softening, which implies that their mechanical response primarily relies on time and on the maximum deformation experienced. From a macroscopic point of view, depending on the quantity and orientation of the fibers, the tissues can present anisotropy (Egan, 1987). Consequently, in an initial approximation, hyperelasticity was employed to describe soft tissues (Chagnon et al., 2015). In this study, time dependency was not studied and the tests were quasi-static. The diverse mechanical characteristics observed in soft tissues have spurred the development of numerous constitutive formulations tailored to different tissue types.

As we have not measured anisotropy of the tissue, but observed the fiber direction for muscles, we compare six hyperelastic models as in (Martins et al., 2006): Yeoh (Yeoh, 1993), Mooney–Rivlin (Mooney, 1940), Ogden (Ogden and Hill, 1997), Humphrey (Humphrey and Yin, 1987), Veronda–Westmann (Veronda and Westmann, 1970) and Martins (Martins et al., 1998). All models assume material isotropy except the Martins model which assumes fiber orientation in the direction of the stretch. Incompressibility constraint is also assumed (Martins et al., 2006).

The definition of a hyperelastic material model starts from the gradient deformation tensor $\mathbf{F}$ which is defined, in the case of material incompressibility and uniaxial tension by:

$$[\mathbf{F}] = \begin{bmatrix} \lambda & 0 & 0 \\ 0 & \lambda^{-\frac{1}{2}} & 0 \\ 0 & 0 & \lambda^{-\frac{1}{2}} \end{bmatrix} \tag{1}$$

where λ is the principal stretch along the loading direction $\hat{x}_1$.

The Right Cauchy–Green tensor $\mathbf{C}$ is defined by $\mathbf{C} = \mathbf{F}^T\mathbf{F}$.

The invariants of the Right Cauchy–Green tensor take the form:

$$\begin{aligned} I_1 &= \mathrm{tr}(\mathbf{C}) = \lambda^2 + \frac{2}{\lambda} \\ I_2 &= \frac{1}{2}\left[(\mathrm{tr}(\mathbf{C}))^2 - \mathrm{tr}(\mathbf{C}^2)\right] = 2\lambda + \frac{1}{\lambda^2} \\ I_3 &= \det(\mathbf{C}) = 1 \end{aligned} \tag{2}$$

The strain energy functions (SEF), denoted $\Psi_{\#}^{\mathrm{incomp}}$, for the six models under incompressibility assumption, are defined by:

$$\Psi_{\#}^{\mathrm{incomp}} = \Psi_{\#} - p\,(\det(\mathbf{F}) - 1) \tag{3}$$

where p is a Lagrange multiplier enforcing incompressibility constraint and is determined in uniaxial tension from equilibrium conditions (i.e. $\sigma_2 = \sigma_3 = 0$). $\Psi_{\#}$ are SEF defined for $\det(\mathbf{F}) = 1$, using for comparison convenience the notation in (Martins et al., 2006):

Mooney–Rivlin (Mooney, 1940) The Mooney–Rivlin model has been widely used in the analysis of rubber components with medium deformation. Its general SEF depends on the invariants I_1 and I_2.

$$\Psi_{\mathrm{MR}} = C_1(I_1 - 3) + C_2(I_2 - 3) \tag{4}$$

Yeoh (Yeoh, 1993) The Yeoh material model was first presented for incompressible (rubber-like) materials. Its SEF only depends on the invariant I_1:

$$\Psi_{\mathrm{Y}} = C_1(I_1 - 3) + C_2(I_1 - 3)^2 + C_3(I_1 - 3)^3 \tag{5}$$

Ogden (Ogden and Hill, 1997) Ogden proposed to derive the strain energy function in terms of generalized strain. The Ogden model can be utilized in a wide strain range with great flexibility. It depends on the principal stretch values λ_1, λ_2 and λ_3.

$$\Psi_{\mathrm{O}} = \sum_{i=1}^{3} \frac{C_{2i-1}}{C_{2i}}[\lambda_1^{C_{2i}} + \lambda_2^{C_{2i}} + \lambda_3^{C_{2i}} - 3] \tag{6}$$

Humphrey (Humphrey and Yin, 1987) This model was proposed to study of passive myocardium. Restricted to isotropic modelling, it depends only on I_1.

$$\Psi_{\mathrm{H}} = C_1 \left(e^{C_2(I_1-3)} - 1 \right) \tag{7}$$

Veronda–Westmann Veronda and Westmann (1970) introduced a hyperelastic material model based on uniaxial tests performed upon skin of cats. Its SEF depends on I_1 and I_2.

$$\Psi_{\mathrm{VW}} = C_1 \left(e^{C_2(I_1-3)} - 1 \right) - \frac{C_1 C_2}{2}(I_2 - 3) \tag{8}$$

Martins (Martins et al., 1998) Martins proposed this model to study skeletal muscles. Although inspired on the Humphrey model (Humphrey and Yin, 1987), this model exhibits an explicit dependence on the fibers stretch (λ_f) which in our case is assumed to correspond to the uniaxial tension direction λ.

$$\Psi_{\mathrm{M}} = C_1 \left(e^{C_2(I_1-3)} - 1 \right) + C_3 \left(e^{C_4(\lambda-1)^2} - 1 \right) \tag{9}$$

For all these models, $C_\#$ represent the material parameters to be identified.

The parameters were identified by solving an inverse problem based on the experimental stress corresponding to the first Piola–Kirchhoff stress and the imposed stretch. To do this, we solved a least squares method using the Levenberg–Marquardt algorithm (Gill and Murray, 1978) before the initial signs of damage appeared in each tissue sample. The damage is associated with the yield point on the experimental curve and indicates fiber rupture or delamination in the tissue as illustrated in Fig. 3 (Korhonen et al., 2011; Fuller and Kirby, 2013; Morch et al., 2020; Yasenchuk et al., 2021). We developed an algorithm to automatically detect the damage initiation point by calculating the first derivative computed by finite difference of the experimental curve and identifying its first maximum.

For each curve, the parameters were then calculated by minimizing the cost function , utilizing the Scipy library (Virtanen et al., 2020):

$$F(\Pi, y) = \frac{1}{n} \sum_{i=1}^{n} (\Pi_i - y_i)^2 \tag{10}$$

where Π and y represent the numerical and the experimental first Piola–Kirchhoff stress values, respectively, for the complete set of n observed stretch values λ_i in the stress–stretch curve. For each sample, the Pearson correlation coefficient, denoted r and defined in Eq. (11), and the p-value with the null hypothesis that there was no correlation between the experimental and numerical stresses were computed.

$$r = \frac{\sum_{i=1}^{n} (\Pi_i - m_\Pi)(y_i - m_y)}{\sqrt{\sum_{i=1}^{n} (\Pi_i - m_\Pi)^2 \sum_{i=1}^{n} (y_i - m_y)^2}} \tag{11}$$

where Π and y are defined above, m_Π and m_y are the means of Π and y.

3. Results

The detection of the damage initiation point in the samples is illustrated in the Fig. 4. The red dot marks the yield point. Material parameters are identified on the stress–stretch curve up to this point.

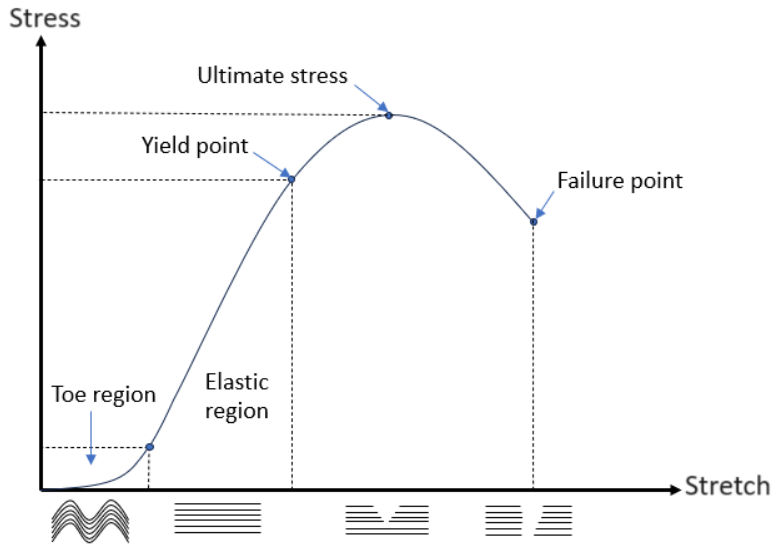

Figure 3: Typical stress–stretch curves for soft biological tissues for a uniaxial tensile test (Korhonen et al., 2011; Morch et al., 2020). For each region, the appearance of the sample fibers is shown: loose in the toe region, stretched in the elastic region, from the yield point damage starts and finally all fibers are broken at the failure point.

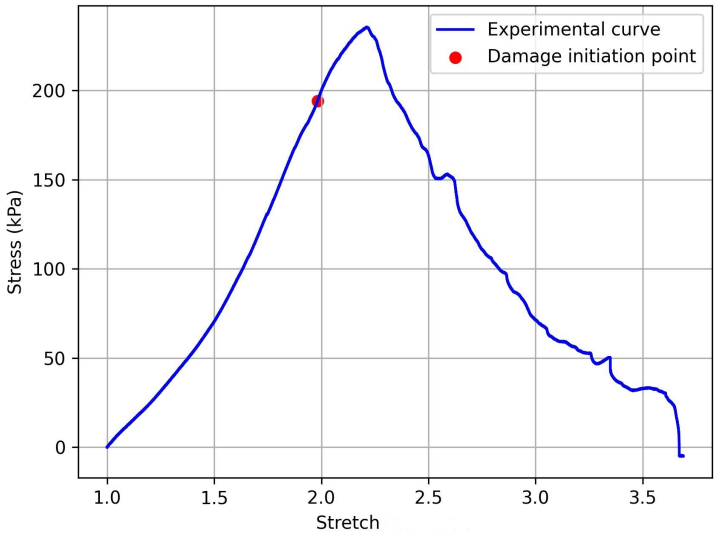

Figure 4: First Piola–Kirchhoff stress P versus imposed stretch λ for an EAS sample under tension after preload. Red point corresponds to the first maximum of $P'(\lambda)$ (i.e. $P''(\lambda) = 0$) called yield point and assumed to be the damage initiation load.

The truncated experimental curves for each tissue are presented in the figures below (Fig. 5). From the experimental data, we noted a high variability in the samples. This was particularly present for the skin, EAS and IAS. On five curves we also noticed a negligible drop in stress which might be caused by a small slip of the sample from the grips. The mean stretch and stress for all tissues before the damage initiation point on the stress–stretch curve are also given in Table 1.

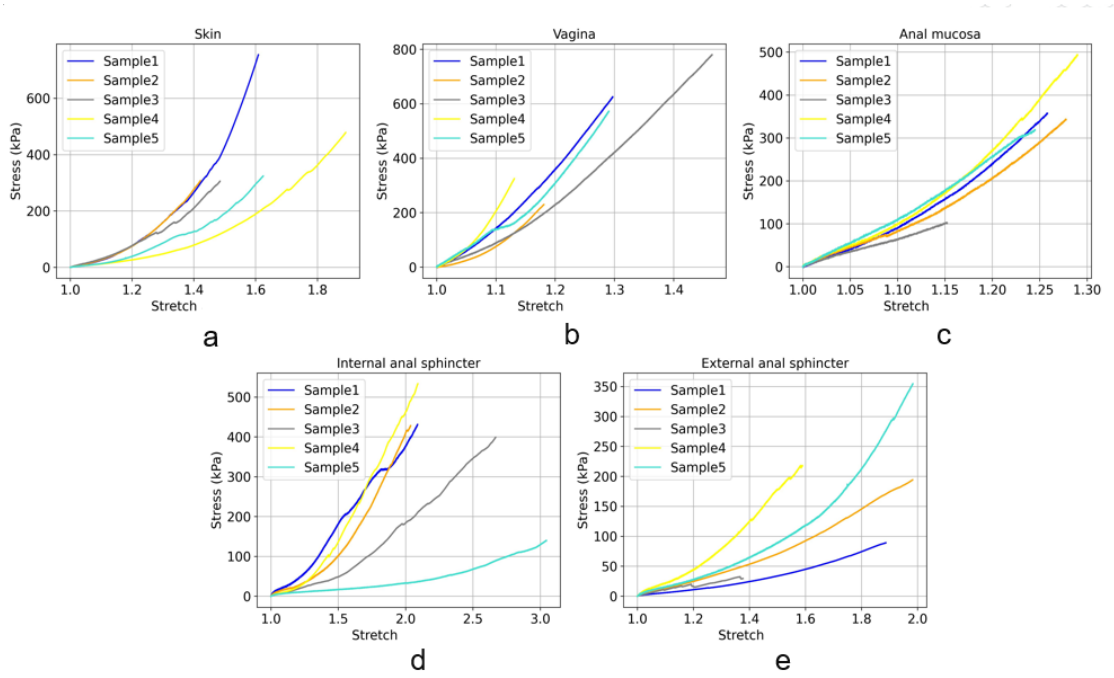

Figure 5: First Piola–Kirchhoff stress versus imposed stretch, up to yield point, for dissected parts (Skin, Vagina, Anal Mucosa, Internal Anal Sphincter, External Anal Sphincter) of five sow perineums.

Table 1: Maximum stress and stretch before damage for each tissue (mean ± standard deviation).

	Skin	Vagina	EAS	AM	IAS
Stretch (%)	56 ± 16	24 ± 10	72 ± 35	22 ± 9	115 ± 50
Stress (kPa)	582 ± 316	523 ± 228	272 ± 209	282 ± 158	432 ± 192

The correlation coefficients for each model of each tissues are presented in the Fig. 6. All correlation coefficients are greater then 0.95 with extremely low p-value ($< 10^{-8}$) meaning the results were statistically significant. From the values of the correlation coefficients, AM samples showed the best results with all the models. This might be due to the quasi-linear response of that tissue. There was a similar observation for the vaginal tissues. For all tissues, the Yeoh and Martins models showed the highest correlation coefficients. The Mooney–Rivlin and the Veronda–Westmann models displayed the lowest ones.

For further results, we took a look at the number of iterations to get the optimal parameters as well as the value of the cost function at the solution (Table 2).

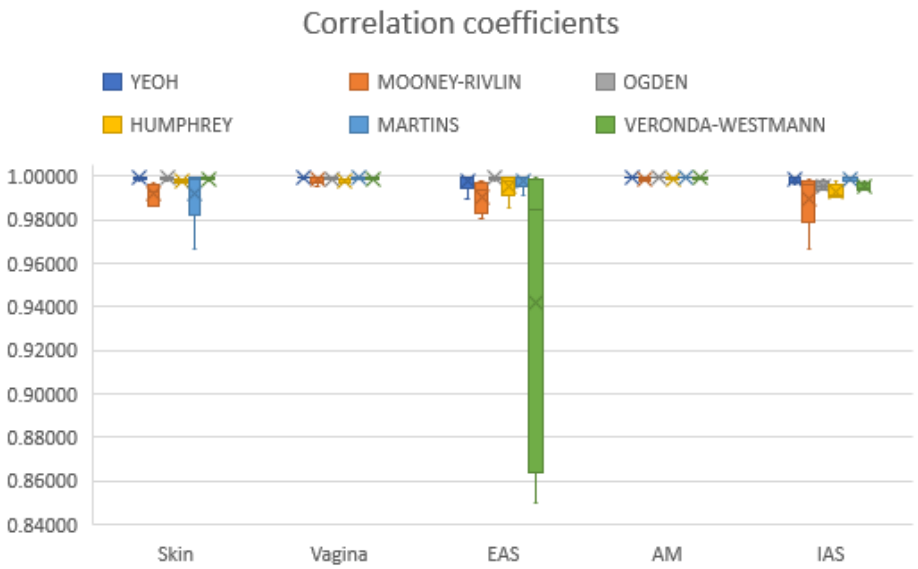

Figure 6: Correlation coefficients of experimental versus numerical first Piola–Kirchhoff stress (Eq. (11)) for dissected parts (skin, vagina, anal mucosa, External anal sphincter, internal anal sphincter) of five sow perineums. Numerical stresses are computed for six materials models : Yeoh, Mooney–Rivlin, Ogden, Humphrey, Martins, Veronda–Westmann.

Table 2: Number of iterations and cost function at the solution for all models: mean and standard deviation (SD).

		Nb of iterations					Cost function at solution (kPa)				
		Skin	Vagina	EAS	AM	IAS	Skin	Vagina	EAS	AM	IAS
Yeoh	Mean	9	15	10	13	11	21.32	17.33	1.90	4.56	32.85
	SD	0	2	2	0	2	23.67	25.48	1.39	3.53	47.63
Mooney–Rivlin	Mean	14	17	9	15	10	383.17	63.86	84.93	31.22	139.08
	SD	1	2	3	3	2	487.73	117.50	158.27	29.88	95.19
Ogden	Mean	1065	109	217	114	116	21.74	70.82	5.28	11.90	188.91
	SD	1329	51	159	63	55	10.74	83.44	6.04	9.57	139.60
Humphrey	Mean	44	42	103	64	54	68.01	138.13	11.08	20.69	309.88
	SD	4	18	126	27	5	45.59	165.77	12.61	21.81	250.63
Veronda–Westmann	Mean	40	55	878	1391	66	32.03	79.94	665.74	10.96	192.39
	SD	19	20	1846	2961	16	18.83	82.94	1377.61	9.51	162.34
Martins	Mean	181	1262	3624	218	6589	34.32	38.14	1.45	2.95	26
	SD	180	1666	7323	269	8853	25.42	52.84	1.32	2.37	22.12

From this data, we noticed that, for the Yeoh and Mooney–Rivlin models, the algorithm was able to converge to a solution with a mean of less then 15 iterations. Next came the Humphrey with an average of 62 iterations. Then we had the Ogden model with 324 iterations followed by the Veronda–Westmann with 486 iterations and lastly the Martins model with an average of 2375 iterations. Regarding the values of the cost function (Eq. (10)), they were low for the Yeoh and Martins models for all tissues. Looking at all models for the skin, the Yeoh model converged with the smallest value of the cost function followed by the Ogden, Veronda–Westmann and Martins models. The Mooney–Rivlin model had the highest value of the cost function (more than 50% error relative to the maximum stress of the experimental curve) even though it had reached a solution with few iterations. The fitting of the models is illustrated in Fig. 7. The same was observed with the EAS for which the Yeoh and Martins models are equivalent and followed closely by the Ogden model. For the vagina, the Martins and Yeoh models again obtained the smallest values at the cost function while the Veronda–Westmann and Humphrey models reached a solution with a high error. Similar to the results of the correlation coefficients, the values of the cost function were low for all tissues, again due to the quasi-linear experimental curves. The IAS seemed the hardest to fit for all models with the highest values of the cost function. Apart from the Yeoh and Martins models, the other models converged with more then 50% error of the cost function.

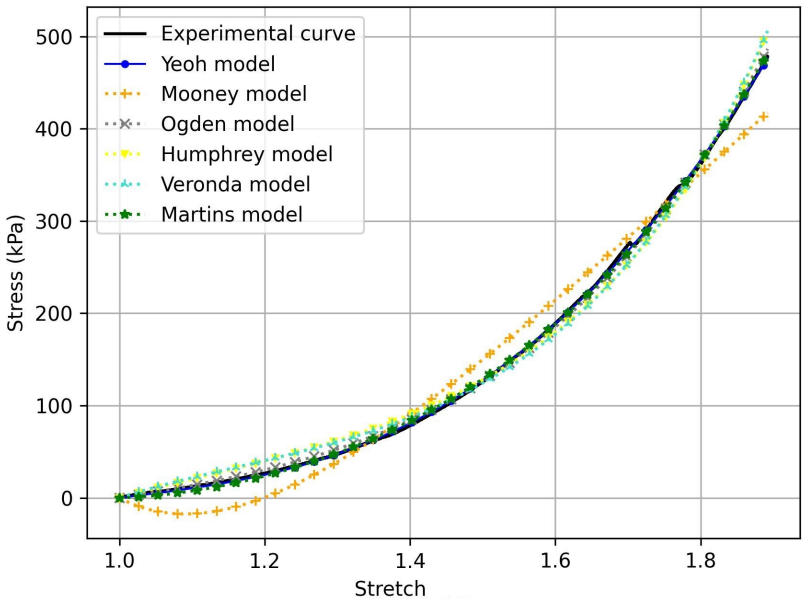

Figure 7: Experimental and fitted First Piola–Kirchhoff stress versus stretch curves for skin sample 4 (Fig. 5) under tension. Fitted curves are obtained from six hyperelastic models with incompressible assumption: Mooney–Rivlin model (Eq. (4), C_1 = 353.08 kPa, C_2 = −423.16 kPa), Yeoh (Eq. (5), C_1 = 17.06 kPa, C_2 = 35.51 kPa, C_3 = 1.78 kPa), Ogden (Eq. (6), C_1 = 3.71 kPa, C_2 = 6.72 kPa, C_3 = 4.34 kPa, C_4 = 6.72 kPa, C_5 = 4.65 kPa, C_6 = 6.72 kPa), Humphrey (Eq. (7), C_1 = 39.71 kPa, C_2 = 0.9 kPa), Veronda–Westmann (Eq. (8) C_1 = 69.84 kPa, C_2 = 0.73 kPa) and Martins (Eq. (9) C_1 = 26.76 kPa, C_2 = 1.46 kPa, C_3 = 3.64 kPa, C_4 = −7.77 kPa).

From the correlation coefficients and cost function at the solution values, the ranking of the models from best fit to worst fit are reported in Table 3. The corresponding material parameters are reported in Tables A.5 to A.9.

Table 3: Ranking of the material models for each tissue (++: best fit; +−: good fit; −−: worst fit).

		Skin	Vagina	EAS	AM	IAS
Yeoh	Correlation coefficient	++	++	++	++	+−
	Cost function	++	++	++	++	+−
Mooney–Rivlin	Correlation coefficient	−−	+−	−−	++	−−
	Cost function	−−	+−	−−	+−	−−
Ogden	Correlation coefficient	++	+−	++	++	+−
	Cost function	++	+−	++	++	−−
Humphrey	Correlation coefficient	+−	+−	+−	++	+−
	Cost function	+−	−−	+−	+−	−−
Veronda–Westmann	Correlation coefficient	++	+−	−−	++	+−
	Cost function	++	+−	−−	++	−−
Martins	Correlation coefficient	++	++	++	++	+−
	Cost function	++	++	++	++	+−

4. Discussion

A protocol for the biomechanical characterization of perineal porcine tissues was developed using uniaxial tensile tests in the general fiber direction of the samples. The focus of the study was the comparison of several material models to determine which best fits the experimental data for each of soft tissues of the perineum that was dissected: skin, vagina, external anal sphincter, internal anal sphincter and anal mucosa.

The results proved the non-linear hyperelastic behaviour of the different tissues of the porcine perineum. The comparison of some existing hyperelastic models showed that the Yeoh, Martins and Ogden models described the behaviour of the tissues better then the Mooney–Rivlin, Humphrey and Veronda–Westmann models. However, the Ogden model was unable to fit all the curves of all tissues. Moreover, high values of the cost function at the solution for the Mooney–Rivlin, Humphrey and Veronda–Westmann models indicate that the algorithm was not able to fit the experimental data. This was especially noticeable for the Mooney–Rivlin model for which we have a small number of iterations for a high cost function value (illustrated in Fig. 7). Most Mooney–Rivlin parameters obtained by solving an unconstrained inverse problem violate the stability condition ($C_1 + C_2 > 0$) (Drucker, 1956). Hence, as observed on Fig. 7, increasing the stretch value leads to a decrease of stress. So, an identification of Mooney–Rivlin parameters under the stability condition constraints has been realized. However, in this case, cost function values were worse than those without stability condition (Table A.4). Indeed, Mooney–Rivlin constitutive law is not adapted to model perineal soft tissues. As parameter identification was realized with an unconstrained optimization, the stability condition, related to the convexity of $\Psi_{\#}$, is checked looking at the sign of $\Psi''_{\#}$ for all hyperelastic models (Ogden , 2003) (see supplementary Tables A.5 to A.9 in Appendix).

The results concerning the models comparison are in agreement with the study of (Martins et al., 2006) in which the material models were compared on porcine muscle. It was found that the Yeoh, Ogden and Martins models presented a very good description of the material properties

of soft biological tissues. Another similar study on pig skin from the spine and stomach regions reached the same conclusion with an emphasis that Mooney–Rivlin and Veronda–Westmann models were the least accurate models (Łagan and Liber-Kneć, 2017). Moreover, a comparison of the Yeoh, Mooney–Rivlin and Ogden models on pig skin (belly and back) confirmed that the Yeoh model captures accurately the behaviour of the pig skin (Dwivedi et al., 2022). It also highlighted the stability issues that arise when using the Ogden model as well as the failure of the Mooney–Rivlin model to properly describe the behaviour of the tissues.

Despite the good results obtained, there are various limitations associated with our study. One of these limitations comes from the non-homogeneity and the irregularity in thickness of some samples such as the skin and the EAS. This is due to the difference in skin texture around the vulva and the ano-vulvar region of the perineum. A second reason is that the EAS is too small to extract samples and thus must be taken as is to test. Additionally, there is some uncertainty associated to the computation of the section of the samples which are not perfectly rectangular. Moreover, there is a lack of information on the precise fiber orientation of the tissues. These limitations lead to a high variability in the response of the tissues (Tables A.5 to A.9) as well as non homogeneous strain fields within the samples. The use of digital image correlation could counteract these problems to have a better understanding of the properties of these tissues.

Another limitation of this study with regards to the use of the results for humans is the anatomical differences between the porcine and human perineum. The human perineum has more layers than the sow perineum. Indeed, there are no perineal muscles and so no perineal body (central attachment of the perineal muscles). Moreover, with the human and porcine posture being different, we would assume that the human perineum is subjected to more stress.

To pursue the investigation of the mechanical properties of the perineal tissues, it is important to consider the remaining part of the stress–stretch experimental data by introducing a damage criterion with the material model. Failure analysis is important for these tissues as the ultimate objective is to understand the rupture of the perineum during childbirth (Calvo et al., 2009; Ferreira et al., 2017; Li, 2016; Martins et al., 2012). Moreover, the anisotropy of the tissues need to be investigated as well as the viscous behaviour. Lakhani et al. (2020) studied the anisotropy of the porcine skin from multiple locations of the pig and found the angle of maximum and minimum elastic modulus as well as the collagen orientation intensity. Shi et al. (2019) characterized, by finite element model updating, anisotropic material properties of human cervical tissues from indentation and video extensometry measurements. Their model takes into account fiber orientation measured using Optical Coherence Tomography. Peña et al. (2011) studied the anisotropy and viscoelastic behaviour of human vaginal tissues and proposed a constitutive model that may be useful for further studies on the porcine perineum. Ferreira et al. (2017) also developed a numerical framework including non-local damage to describe hyperelastic constitutive laws. These more complete material models could allow us to build a computational model of the porcine perineum which would be validated on experimental tests on the entire perineum simulating childbirth. This is a step towards a computational model of the human perineum in which the material properties would be obtained from in-vivo measurements.

5. Conclusion

Porcine perineums were dissected and tissues such as the skin, vagina, external anal sphincter (EAS), internal anal sphincter (IAS) and anal mucosa (AM) were subjected to uniaxial tensile tests. This paper is one of the first to investigate these different tissues seperately. A testing and analysis methodology was developed and multiple hyperelastic constituve laws were compared.

The results of this preliminary study give an insight on the mechanical behaviour of those tissues. Despite the variability of the response for each tissue, there is a clear difference in curve shape, stiffness and yield point between the five tissues. The Yeoh and Martin models described accurately the behaviour of all the different tissues. For further studies, the Yeoh model is a good compromise between accuracy, correlation and computation cost for the hypothesis of isotropy. These preliminary results must be completed by carrying out an experimental campaign on a larger number of samples in order to first build an experimental database and to study the effect of environmental and experimental conditions on the material properties of the porcine perineal tissues. This study is the first step towards understanding the mechanical behaviour of the perineum and its different tissues for the prediction of the damage and tear during childbirth.

Acknowledgements

This work has been achieved in the frame of the EIPHI Graduate school (contract ANR-17-EURE-0002) and supported by the 'Region Bourgogne Franche-Comté' (convention 2020-7-21503). The authors would like to show gratitude to the 'Etablissement Français du Sang' for hosting the equipment and experiments on their premises.

Appendix A. Tables

See Tables A.4–A.9.

Table A.4: Results for the Mooney–Rivlin model with unconstrained and constrained parameters.

		Unsconstrained				Constrained			
		C_1 (kPa)	C_2 (kPa)	Cost function (kPa)	r	C_1	C_2	Cost function (kPa)	r
Skin	Mean	510.68	−554.69	383.17	0.992	417.92	−416.79	826.77	0.986
	SD	221.55	252.26	487.73	0.005	160.05	160.13	1055.24	0.010
Vagina	Mean	1800.83	−1728.67	63.86	0.999	1796.58	−1723.82	63.90	0.999
	SD	921.19	923.87	117.5	0.002	922.40	924.77	117.48	0.002
EAS	Mean	125.49	−127.94	84.93	0.991	115.29	−110.42	127.14	0.989
	SD	94.69	106.39	158.27	0.008	87.19	90.80	251.72	0.011
AM	Mean	840.91	−745.02	31.22	0.999	840.91	−745.02	31.22	0.999
	SD	431.90	455.66	29.88	0.001	431.90	455.66	29.88	0.001
IAS	Mean	191.33	−215.87	139.08	0.990	158.39	−154.01	426.75	0.984
	SD	110.16	128.32	95.19	0.013	88.56	86.60	316.44	0.017

Table A.5: Material parameters (mean and standard deviation in kPa) of skin tissues for all models using unconstrained optimization. $\Psi''_{\#}$ is the second derivative of the SEF and is checked for convexity.

		C_1	C_2	C_3	C_4	C_5	C_6	$\Psi''_{\#}$
Yeoh	Mean	40.69	83.34	5.14				> 0
	SD	17.38	53.70	31.74				
Mooney–Rivlin	Mean	510.68	−554.69					< 0
	SD	221.55	252.26					
Ogden	Mean	3.56	11.85	9.71	7.48	7.99	12.75	> 0
	SD	2.58	9.44	5.46	0.90	8.50	12.13	
Humphrey	Mean	35.69	1.60					> 0
	SD	7.55	0.58					
Veronda–Westmann	Mean	75.88	1.16					> 0
	SD	18.76	0.39					
Martins	Mean	26.85	2.34	8.10	−3.53			> 0
	SD	7.04	1.13	3.86	2.57			

Table A.6: Material parameters (mean and standard deviation in kPa) of vagina tissues for all models using unconstrained optimization. $\Psi''_{\#}$ is the second derivative of the SEF and is checked for convexity.

		C_1	C_2	C_3	C_4	C_5	C_6	$\Psi''_{\#}$
Yeoh	Mean	162.77	1145.56	−4116.94				> 0
	SD	61.88	1646.08	74.14.71				
Mooney–Rivlin	Mean	1800.83	−1728.67					> 0
	SD	921.19	923.87					
Ogden	Mean	23.54	12.12	23.78	12.12	24.49	12.12	> 0
	SD	16.55	5.98	16.52	5.98	15.58	5.98	
Humphrey	Mean	70.15	6.75					> 0
	SD	61.13	6.35					
Veronda–Westmann	Mean	212.37	4.79					> 0
	SD	210.50	4.42					
Martins	Mean	−26.71	28.91	73.47	66.97			> 0
	SD	96.81	28.08	71.94	114.30			

Table A.7: Material parameters (mean and standard deviation in kPa) of EAS tissues for all models using unconstrained optimization. $\Psi''_{\#}$ is the second derivative of the SEF and is checked for convexity.

		C_1	C_2	C_3	C_4	C_5	C_6	$\Psi''_{\#}$
Yeoh	Mean	22.15	12.68	4.55				> 0
	SD	8.63	28.38	19.58				
Mooney–Rivlin	Mean	125.49	−127.94					< 0
	SD	94.69	106.39					
Ogden	Mean	5.91	5.69	9.52	4.24	10.17	4.24	> 0
	SD	3.65	1.25	7.32	1.86	12.33	1.86	
Humphrey	Mean	123.53	0.54					> 0
	SD	180.50	0.35					
Veronda–Westmann	Mean	84.15	−2.80					> 0
	SD	66.60	3.87					
Martins	Mean	20.42	1.39	4.52	7.77			> 0
	SD	20.96	1.20	2.88	19.74			

Table A.8: Material parameters (mean and standard deviation in kPa) of AM tissues for all models using unconstrained optimization. $\Psi''_{\#}$ is the second derivative of the SEF and is checked for convexity.

		C_1	C_2	C_3	C_4	C_5	C_6	$\Psi''_{\#}$
Yeoh	Mean	146.24	317.27	405.01				> 0
	SD	20.07	359.85	1705.57				
Mooney–Rivlin	Mean	840.91	−745.02					> 0
	SD	431.90	455.66					
Ogden	Mean	28.68	8.32	25.23	8.32	22.84	8.32	> 0
	SD	7.36	1.40	9.73	1.40	11.24	1.40	
Humphrey	Mean	66.41	2.68					> 0
	SD	25.17	1.00					
Veronda–Westmann	Mean	203.95	1.68					> 0
	SD	107.06	0.50					
Martins	Mean	86.23	6.89	20.38	−73.66			> 0
	SD	48.28	0.61	4.84	61.70			

Table A.9: Material parameters (mean and standard deviation in kPa) of IAS tissues for all models using unconstrained optimization. $\Psi''_{\#}$ is the second derivative of the SEF and is checked for convexity.

		C_1	C_2	C_3	C_4	C_5	C_6	$\Psi''_{\#}$
Yeoh	Mean	19.73	24.38	−2.76				> 0
	SD	16.18	18.76	2.89				
Mooney–Rivlin	Mean	191.33	−215.87					< 0
	SD	110.16	128.32					
Ogden	Mean	12.63	4.54	10.24	4.53	11.67	4.54	> 0
	SD	12.11	0.93	7.28	0.93	4.56	0.93	
Humphrey	Mean	143.30	0.33					> 0
	SD	115.44	0.18					
Veronda–Westmann	Mean	181.23	0.24					> 0
	SD	111.92	0.15					
Martins	Mean	66.30	−1.48	0.20	1138.66			> 0
	SD	59.07	1.81	0.15	1839.33			

References

Brieu, M., Chantereau, P., Gillibert, J., de Landsheere, L., Lecomte, P., Cosson, M., 2016. A nonlinear-elastic constitutive model for soft connective tissue based on a histologic description: Application to female pelvic soft tissue. Journal of the Mechanical Behavior of Biomedical Materials 58, 65–74.

Calvo, B., Peña, E., Martins, P., Mascarenhas, T., Doblaré, M., Natal Jorge, R.M., Ferreira, A., 2009. On modelling damage process in vaginal tissue. Journal of Biomechanics 42, 642–651.

Chagnon, G., Rebouah, M., Favier, D., 2015. Hyperelastic energy densities for soft biological tissues: A review. Journal of Elasticity 120, 129–160.

Chen, L., Low, L.K., DeLancey, J.O., Ashton-Miller, J.A., 2015. In vivo estimation of perineal body properties using ultrasound quasistatic elastography in nulliparous women. Journal of Biomechanics 48, 1575–1579.

Cone, S.G., Warren, P.B., Fisher, M.B., 2017. Rise of the pigs: Utilization of the Porcine model to study Musculoskeletal biomechanics and tissue engineering during skeletal growth. Tissue Engineering. Part C 23, 763–780.

Debeer, S., Le Luduec, J.B., Kaiserlian, D., Laurent, P., Nicolas, J.F., Dubois, B., Kanitakis, J., 2013. Comparative histology and immunohistochemistry of porcine versus human skin. European journal of dermatology 23, 456–66.

DeLancey, J.O., 1999. Structural anatomy of the posterior pelvic compartment as it relates to rectocele. American Journal of Obstetrics and Gynecology 180, 815–823.

Drucker, D.C., 1956. On uniqueness in the theory of plasticity. Quarterly of Applied Mathematics 14, 35–42.

Dwivedi, K.K., Lakhani, P., Kumar, S., Kumar, N., 2022. A hyperelastic model to capture the mechanical behaviour and histological aspects of the soft tissues. Journal of the Mechanical Behavior of Biomedical Materials 126, 105013.

Egan, J.M., 1987. A constitutive model for the mechanical behaviour of soft connective tissues. Journal of Biomechanics 20, 681–692.

Ferreira, J., Parente, M., Jabareen, M., Natal Jorge, R., 2017. A general framework for the numerical implementation of anisotropic hyperelastic material models including non-local damage. Biomechanics and Modeling in Mechanobiology 16, 1119–1140.

Friis, S.J., Hansen, T.S., Poulsen, M., Gregersen, H., Brüel, A., Vinge Nygaard, J., 2023. Biomechanical properties of the stomach: A comprehensive comparative analysis of human and porcine gastric tissue. Journal of the Mechanical Behavior of Biomedical Materials 138, 105614.

Fuller, E., Kirby, K., 2013. Subtalar joint equilibrium and tissue stress approach to biomechanical therapy of the foot and lower extremity. In: Lower Extremity Biomechanics: Theory and Practice Vol. 1, pp. 205–264.

Gill, P.E., Murray, W., 1978. Algorithms for the solution of the nonlinear least-squares problem. SIAM Journal on Numerical Analysis 15, 977–992.

Goh, R., Goh, D., Ellepola, H., 2018. Perineal tears – A review. Australian Journal of General Practice 47, 35–38.

Holzapfel, G., Gasser, T., Ogden, R., 2000. A new constitutive framework for arterial wall mechanics and a comparative study of material models. Journal of Elasticity 61, 1–48.

Gruber, D. D., Warner, W. B., Lombardini, E. D., Zahn, C. M., Buller, J. L., 2011. Anatomical and histological examination of the porcine vagina and supportive structures: in search of an ideal model for pelvic floor disorder evaluation and management. Urogynecology 17, 110–114.

Humphrey, J.D., Yin, F.C., 1987. On constitutive relations and finite deformations of passive cardiac tissue: I. A pseudostrain-energy function. Journal of Biomechanical Engineering 109, 298–304.

Jing, D., Ashton-Miller, J.A., DeLancey, J.O.L., 2012. A subject-specific anisotropic visco-hyperelastic finite element model of female pelvic floor stress and strain during the second stage of labor. Journal of Biomechanics 45, 455–460.

Korhonen, R.K., Saarakkala, S., Korhonen, R.K., Saarakkala, S., 2011. Biomechanics and modeling of skeletal soft tissues, In: Theoretical Biomechanics. IntechOpen.

Łagan, S.D., Liber-Kneć, A., 2017. Experimental testing and constitutive modeling of the mechanical properties of the swine skin tissue. Acta of Bioengineering and Biomechanics 19, 93–102.

Lakhani, P., Dwivedi, K.K., Kumar, N., 2020. Directional dependent variation in mechanical properties of planar anisotropic porcine skin tissue. Journal of the Mechanical Behavior of Biomedical Materials 104, 103693.

Larson, K.A., Yousuf, A., Lewicky-Gaupp, C., Fenner, D.E., DeLancey, J.O., 2010. Perineal body anatomy in living women: 3-dimensional analysis using thin-slice magnetic resonance imaging. American Journal of Obstetrics and Gynecology 203, 494.e15–494.e21.

Li, W., 2016. Damage models for soft tissues: A survey. Journal of Medical and Biological Engineering 36, 285–307.

MacManus, D. B., Menichetti, A., Depreitere, B., Famaey, N., Vander Sloten, J., Gilchrist, M., 2020. Towards animal surrogates for characterising large strain dynamic mechanical properties of human brain tissue. Brain Multiphysics 1, 100018.

Martins, J., Pires, E., Salvado, R., Dinis, P., 1998. A numerical model of passive and active behavior of skeletal muscles. Computer Methods in Applied Mechanics and Engineering 151, 419–433.

Martins, P., Natal Jorge, R.M., Ferreira, A.J.M., 2006. A comparative study of several material models for prediction of hyperelastic properties: Application to silicone-rubber and soft tissues. Strain 42, 135–147.

Martins, P., Peña, E., Jorge, R.M.N., Santos, A., Santos, L., Mascarenhas, T., Calvo, B., 2012. Mechanical characterization and constitutive modelling of the damage process in rectus sheath. Journal of the Mechanical Behavior of Biomedical Materials 8, 111–122.

Mooney, M., 1940. A theory of large elastic deformation. Journal of Applied Physics 11, 582–592.

Morch, A., Astruc, L., Mayeur, O., Witz, J.F., Lecomte-Grosbras, P., Brieu, M., 2020. Is there any objective and independent characterization and modeling of soft biological tissues? Journal of the Mechanical Behavior of Biomedical Materials 110, 103915.

Navindaran, K., Kang, J.S., Moon, K., 2023. Techniques for characterizing mechanical properties of soft tissues. Journal of the Mechanical Behavior of Biomedical Materials 138, 105575.

Ogden, R.W., 2003. Nonlinear elasticity, anisotropy, material stability and residual stresses in soft tissue. In: Biomechanics of Soft Tissue in Cardiovascular Systems, 65–108.

Ogden, R.W., Hill, R., 1997. Large deformation isotropic elasticity – on the correlation of theory and experiment for incompressible rubberlike solids. Proceedings of the Royal Society of London. A. Mathematical and Physical Sciences 326, 565–584.

Parente, M., Jorge, R.M.N., Mascarenhas, T., Fernandes, A.A., Martins, J.a.C., 2008. Deformation of the pelvic floor muscles during a vaginal delivery. International Urogynecology Journal and Pelvic Floor Dysfunction 19, 65–71.

Parente, M., Natal Jorge, R.M., Mascarenhas, T., Fernandes, A.A., Silva-Filho, A.L., 2010. Computational modeling approach to study the effects of fetal head flexion during vaginal delivery. American Journal of Obstetrics and Gynecology 203, 217.e1–217.e6.

Peña, E., Martins, P., Mascarenhas, T., Natal Jorge, R.M., Ferreira, A., Doblaré, M., Calvo, B., 2011. Mechanical characterization of the softening behavior of human vaginal tissue. Journal of the Mechanical Behavior of Biomedical Materials 4, 275–283.

Ranamukhaarachchi, S.A., Lehnert, S., Ranamukhaarachchi, S.L., Sprenger, L., Schneider, T., Mansoor, I., Rai, K., Häfeli, U.O., Stoeber, B., 2016. A micromechanical comparison of human and porcine skin before and after preservation by freezing for medical device development. Scientific Reports 6, 32074.

Rostaminia, G., Awad, C., Chang, C., Sikdar, S., Wei, Q., Shobeiri, S.A., 2019. Shear wave elastography to assess perineal body stiffness during labor. Female Pelvic Medicine & Reconstructive Surgery 25, 443–447.

Rubod, C., Boukerrou, M., Brieu, M., Dubois, P., Cosson, M., 2007. Biomechanical properties of vaginal tissue. Part 1: new experimental protocol. The Journal of Urology 178, 320–325.

Rubod, C., Boukerrou, M., Brieu, M., Jean-Charles, C., Dubois, P., Cosson, M., 2008. Biomechanical properties of vaginal tissue: preliminary results. International Urogynecology Journal 19, 811–816.

Ruiz-Zapata, A.M., Feola, A.J., Heesakkers, J., de Graaf, P., Blaganje, M., Sievert, K.D., 2018. Biomechanical properties of the pelvic floor and its relation to pelvic floor disorders. European Urology Supplements. 17, 80–90.

Shafik, A., Ahmed, I., Shafik, A.A., El-Ghamrawy, T.A., El-Sibai, O., 2005. Surgical anatomy of the perineal muscles and their role in perineal disorders. Anatomical Science International 80, 167–171.

Shi, L., Yao, W., Gan, Y., Zhao, L. Y., Eugene McKee, W., Vink, J., Wapner, R. J., Hendon, C. P., Myers, K., 2019. Anisotropic material characterization of human cervix tissue based on indentation and inverse finite element analysis. Journal of Biomechanical Engineering 141, 091017.

Strauss, C., Lienemann, A., Spelsberg, F., Bauer, M., Jonat, W., Strauss, A., 2012. Biomechanics of the female pelvic floor: a prospective trail of the alteration of force–displacement-vectors in parous and nulliparous women. Archives of Gynecology and Obstetrics 285, 741–747.

Tan, T., Davis, F.M., Gruber, D.D., Massengill, J.C., Robertson, J.L., De Vita, R., 2015. Histo-mechanical properties of the swine cardinal and uterosacral ligaments. Journal of the Mechanical Behavior of Biomedical Materials 42, 129–137.

Veronda, D.R., Westmann, R.A., 1970. Mechanical characterization of skin—Finite deformations. Journal of Biomechanics 3, 111–124.

Virtanen, P., Gommers, R., Oliphant, T.E., Haberland, M., Reddy, T., Cournapeau, D., Burovski, E., Peterson, P., Weckesser, W., Bright, J., van der Walt, S.J., Brett, M., Wilson, J., Millman, K.J., Mayorov, N., Nelson, A.R.J., Jones, E., Kern, R., Larson, E., Carey, C.J., Polat, İ., Feng, Y., Moore, E.W., VanderPlas, J., Laxalde, D., Perktold, J., Cimrman, R., Henriksen, I., Quintero, E.A., Harris, C.R., Archibald, A.M., Ribeiro, A.H., Pedregosa, F., van Mulbregt, P., SciPy 1.0 Contributors, 2020. SciPy 1.0: Fundamental Algorithms for Scientific Computing in Python. Nature Methods 17, 261–272.

Yasenchuk, Y.F., Marchenko, E.S., Gunter, S.V., Baigonakova, G.A., Kokorev, O.V., Volinsky, A.A., Topolnitsky, E.B., 2021. Softening effects in biological tissues and NiTi knitwear during cyclic loading. Materials 14, 6256.

Yeoh, O.H., 1993. Some forms of the strain energy function for rubber. Rubber Chemistry and Technology 66, 754–771.

Zemčík, R., Karbanova, J., Kalis, V., Lobovský, L., Jansová, M., Rusavy, Z., 2012. Stereophotogrammetry of the perineum during vaginal delivery. International Journal of Gynecology & Obstetrics 119, 76–80.